Supporting Information

Time-resolved X-ray photoelectron spectroscopy: Ultrafast dynamics in CS_2 probed at the S 2p edge

Ian Gabalski,[†] Felix Allum,[¶] Issaka Seidu,[‖] Mathew Britton,[†] Günter Brenner,[⊥] Hubertus Bromberger,[⊥] Mark Brouard,[§] Philip H. Bucksbaum,[†] Michael Burt,[§] James P. Cryan,[†] Taran Driver,[†] Nagitha Ekanayake,[⊥] Benjamin Erk,[⊥] Diksha Garg,[⊥] Eva Gougoula,[⊥] David Heathcote,[§] Paul Hockett,[‖] David M. P. Holland,[@] Andrew J. Howard,[†] Sonu Kumar,[⊥] Jason W. L. Lee,[⊥] Siqi Li,[¶] Joseph McManus,[§] Jochen Mikosch,[△] Dennis Milesevic,[§] Russell S. Minns,[▽] Simon Neville,[‖] Atia Tul Noor,[⊥] Christina C. Papadopoulou,[⊥] Christopher Passow,[⊥] Weronika O. Razmus,[▽] Anja Röder,[††] Arnaud Rouzée,[††] Alcides Simao,[⊥] James Unwin,[§] Claire Vallance,[§] Tiffany Walmsley,[§] Jun Wang,[†] Daniel Rolles,[‡‡] Albert Stolow,[‖] Michael Schuurman,[*,‖] and Ruaridh Forbes[*,¶]

†*Stanford PULSE Institute, SLAC National Accelerator Laboratory, Menlo Park, CA 94025, USA*

‡*Department of Applied Physics, Stanford University, Stanford, CA 94305, USA*

¶*Linac Coherent Light Source, SLAC National Accelerator Laboratory, Menlo Park, CA 94025, USA*

§*Chemistry Research Laboratory, Department of Chemistry, University of Oxford, Oxford, OX1 3TA, UK*

‖*National Research Council Canada, Ottawa, Ontario, K1A 0R6, Canada*

⊥*Deutsches Elektronen-Synchrotron DESY, Notkestr. 85, 22607 Hamburg, Germany*

#*Department of Physics, Stanford University, Stanford, CA 94305, USA*

@*Daresbury Laboratory, Daresbury, Warrington, Cheshire WA4 4AD, UK*

△*Institut für Physik, Universität Kassel, Heinrich-Plett-Straße 40, 34132 Kassel, Germany*

▽*School of Chemistry, University of Southampton, Highfield, Southampton SO17 1BJ, UK*

††*Max-Born-Institute, Max-Born-Straße 2A, 12489 Berlin, Germany*

‡‡*J. R. Macdonald Laboratory, Department of Physics, Kansas State University, Manhattan, Kansas 66506, USA*

¶¶*Department of Physics, University of Ottawa, Ottawa, Ontario, K1N 6N5, Canada*

§§*Department of Chemistry, University of Ottawa, Ottawa, Ontario, K1N 6N5, Canada*

‖‖*NRC-uOttawa Joint Centre for Extreme Photonics, Ottawa, Ontario, K1A 0R6, Canada*

E-mail: michael.schuurman@uottawa.ca; ruforbes@slac.stanford.edu

S1. AIMS Trajectories

The photo-initiated excited state dynamics of CS_2 were simulated using the *ab initio* multiple spawning method (AIMS). The results of this simulation were used previously to simulate the time-resolved molecular-frame photoelectron angular distributions (TR-MFPADs) in a prior work.[1,2] Briefly, initial conditions were obtained from sampling the ground state vibrational distribution and selecting those phase-space points for which the vertical excitation energy was inside the 200 nm (6.2eV) pump-pulse energy bandwidth window (i.e. $\pm$ 0.1 eV). This excitation energy corresponds to initialization of the trajectories on the $^1\Sigma_u$ electronic state. The non-adiabatic simulation included only those electronic states within the energetically relevant singlet manifold (i.e. $\tilde{X}\ ^1\Sigma^+$, $^1\Sigma_u$, $^1\Pi_u$, and $^1\Delta_u$) and only the A$'$ components of the degenerate states, as the non-adiabatic coupling precludes the coupling between the A$'$ and A$''$ states in C_s symmetry. These states correspond to adiabatic states $S_0 - S_4$ at the multi-reference configuration interaction with single excitations (MR-CIS) level of theory employing the ANO(3s2p1d/4s3p1d) atomic basis set. The electronic structure package COLUMBUS was used for these computations.[3] The reader is referred to Ref.[1,2] for a more detailed description of the dynamics.

Each of the initial conditions (and subsequent spawned trajectories) was propagated until the trajectory was determined to have dissociated into a CS and S-atom fragment. From 32 initial conditions, 346 total trajectory basis functions were spawned on the singlet manifold. While the initial phase-space points were sampled from the $v = 0$ density, candidate points were filtered such that the vertical excitation energy to the $^1\Sigma_u$ state fell within the band-

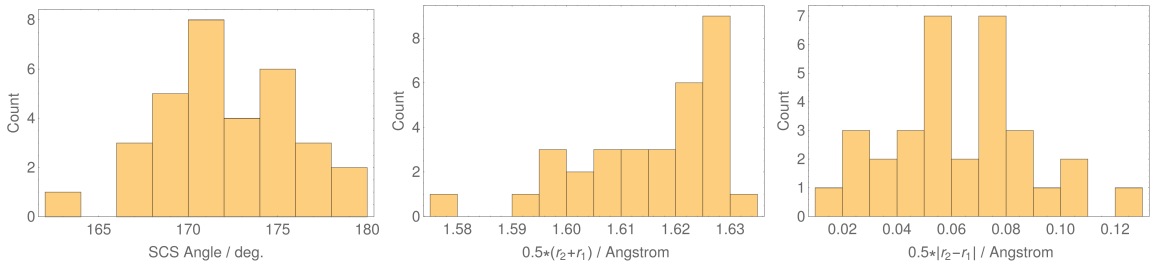

Figure S1: Histogram of the valence internal coordinates of the initially sampled points

width of the excitation pulse. Figure S1 evinces the valence internal coordinates of these points. The filtering process resulted in geometries with significant displacements along each of the internal coordinates, particularly the angle-bend and asymmetric stretch coordinates.

Figure S2 shows the evolution of the adiabatic populations for bound CS_2, where $r_{max} = 1.8$ Å was employed as a cutoff to denote bound molecular species and dissociated fragments. Note further that the adiabatic labels refer only to states within the manifold of A′ states in C_s symmetry; the A′ and A″ manifold cannot be coupled non-adiabatically given then the lack of an A″ symmetry vibrational coordinate.

The initially prepared bright $^1\Sigma_u$ state, here corresponding to the S_2 state in the A′ manifold, rapidly begins to mix with the other electronic states (primarily the Π_g state illustrated in Figure 1(a) in the main text at short times) as evidenced by the mixing of the adiabatic state populations. Concurrent with these non-adiabatic electronic dynamics, CS_2 also begins to dissociate within the singlet manifold, as evinced by the overall decay of population shown in the right panel of Figure S2.

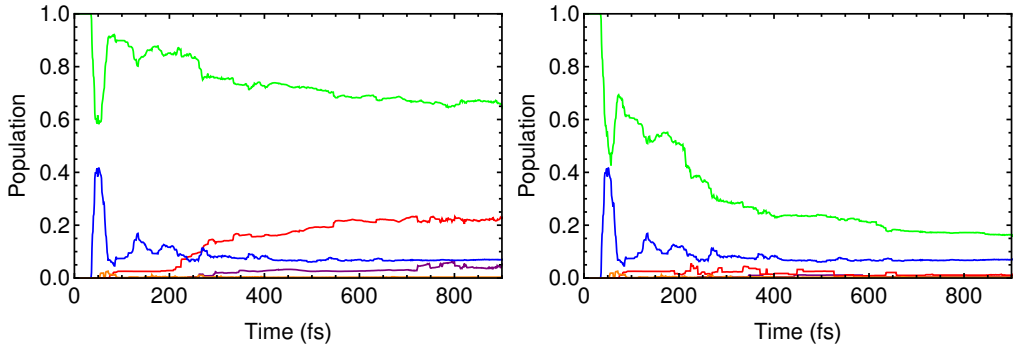

Figure S2: Adiabatic state populations within the A′ manifold of states, where $[S_0,S_1,S_2,S_3,S_4]$ = [purple, red, green, blue, orange] for all trajectories (left) and those corresponding to bound CS_2 (right). At short times, the S_2 state corresponds to the initially prepared $^1\Sigma_u$ state.

The reduced nuclear densities further elucidate the evolution of the nuclear component of the wave packet following photoexcitation. Figure S3 shows the reduced nuclear densities corresponding to the valence angle bend (top panel), the absolute value of an asymmetric stretch coordinate (middle panel), and a symmetric stretch coordinate (bottom panel). These

plots illustrate the coupling between the two large-amplitude displacements that characterize the excited state dynamics of CS_2: angle bend and asymmetric stretch.

Following photoexcitation, the angle bend coordinate undergoes (classically) coherent large amplitude displacement for approximately the first 200 fs, before coupling to the stretch coordinates leads to vibrational dephasing of the wave packet.

Simultaneously, the wave packet evinces large amplitude displacements along the asymmetric stretch mode. The first outer classical turning point is reached within ∼90 fs and corresponds to an $r_{\mathrm{CS}}^{\mathrm{max}}$ of ∼1.85 Å. The equilibrium bond length of the ground state of CS_2 is 1.58 Å. At around this time the wave packet bifurcates and the component that has sufficient internal energy to dissociate continues along this coordinate to dissociate into CS and S products (as shown by the density that extends out to 5 Å), while the remainder returns to C_{2v}-like structures. Note, however, that the return to a displacement of zero along the asymmetric stretch around 180 fs does not correspond to the FC region, but rather, highly bent structures. As the top panel evinces, this time delay corresponds to another classical turning point in which the majority of the wave packet exhibits highly "bent" character, with a maximum in the density observed around 100 degrees.

The evolution of the vibrational component of the wave packet at later times is characterized by a strong mixing of the above discussed internal degrees of freedom. This is communicated in the density plots in Figure S3 as a loss of the classically coherent nuclear motion that characterizes the short-time dynamics. Additionally, the evolution of the nuclear basis functions in the AIMS simulations follows classical equations of motion, and thus, we unsurprisingly see repeated bifurcations between "bound" and "dissociated" CS_2 at the classical turning points of the asymmetric stretch coordinate.

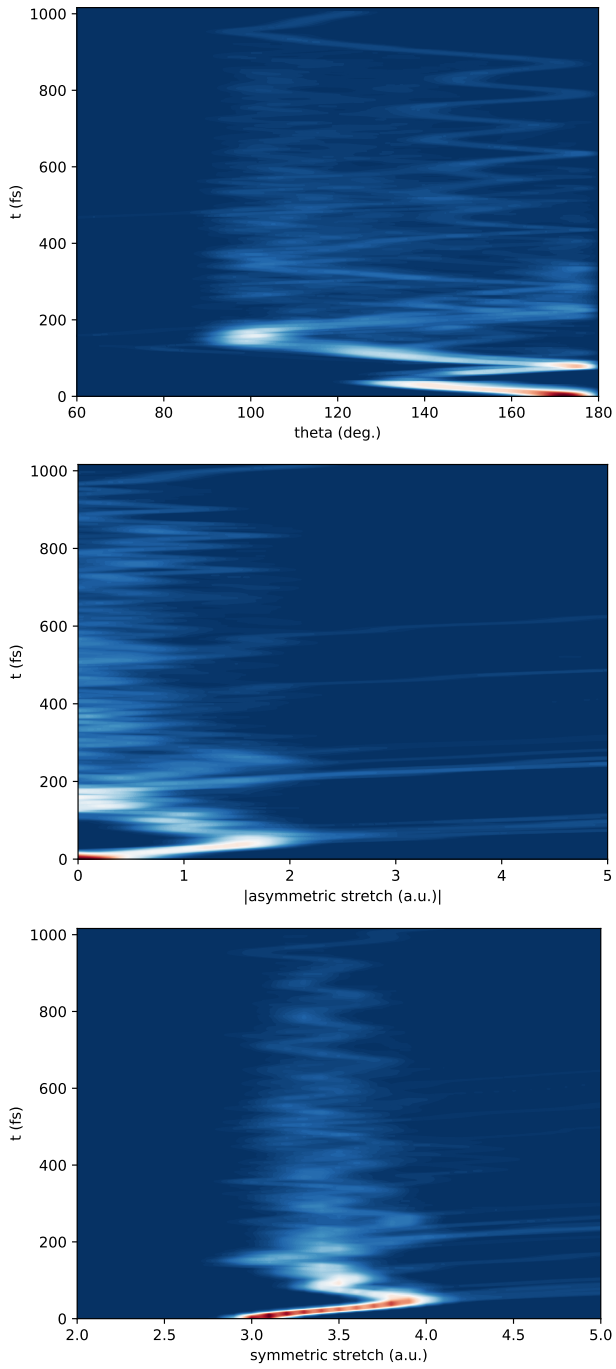

Figure S3: Reduced nuclear densities for simulated CS_2 wave packet, integrated over all electronic states. From top to bottom, the internal coordinates are given by the (i) S-C-S angle bend coordinate (only trajectory basis functions for which $r_{\mathrm{CS}}^{\mathrm{max}} < 2$ Å are included in the density determination), (ii) asymmetric stretch: $r_{CS_1} - r_{CS_2}$, and (iii) symmetric stretch: $0.5 * (r_{CS_1} + r_{CS_2})$.

S2. Simulation of XPS Spectra

The simulation of the X-ray photoelectron spectra employed different levels of theory for the initial (valence excited) and final (core-ionized) electronic states. The initial states were represented at the same level of theory as that employed in the dynamics simulations (ANO(3s2p1d/4s3p1d)//MR-CIS(8,6)), enabling a straightforward simulation of the time-resolved observable by using the exact adiabatic states employed to evolve the nuclear dynamics. The electronic structure of the final (core-ionized) states required a different treatment. The core-ionized states were described with RASCI level of theory with the ANO(3s2p1d/4s3p1d) atomic basis set. The wave functions were constrained to exhibit a single hole in the manifold of the S-atom 2p orbitals (i.e. core-valence separation approximation) and included up to 15 virtual orbitals in the RAS3 space. The MO basis was optimized using a RASSCF procedure in utilizing an (8,6) RAS2 space (corresponding to the CAS space employed in the MR-CIS calculations) as well as the 6 2p orbitals in the RAS1 space. These computations were performed using the MOLCAS electronic structure package.[4] Note that the eKE shift employed for static S-atom spectra in Figures 3 (main text) and S4 was determined from cc-pCVTZ / EOM-CCSD calculations performed using the QChem package.[5]

Given that the 2p orbitals will exhibit potentially observable spin-orbit splitting, the spin-free RASCI states were subsequently used to generate spin-orbit coupled core-ionized states employing the Douglas-Kroll Hamiltonian using the RASSI module in MOLCAS and a corresponding manifold of doublet states. In order to span the spectral range observed in this experiment, up to 100 roots (electronic states) of the spin-orbit coupled RASCI Hamiltonian were determined.

The final element was the determination of the Dyson orbital norms between these initial and final states that are used to approximate the ionization cross-sections. This was achieved by transforming both the singlet valence-excited MR-CIS states and the spin-orbit coupled RASCI states into a common determinantal CI expansion. The wave function overlaps

between these CI expansions were then computed using an in-house developed code.[6]

Static XPS spectra from relevant initial electronic states at key nuclear configurations are shown in Figure S4. The spin-orbit splitting of the 2p orbitals is evinced in each of the spectra and is computed to be ∼1.2 eV. As the left panel shows, the energy of the dominant ionization channels of the initially prepared $^1\Sigma_u$ excited state is expected to overlap strongly with the ground state bleach signal. Indeed, this is observed in the simulated spectrum in Figure 2(b) of the main text as a transient positive signal in the TRXPS at initial times around kinetic energies of 11 eV.

As the molecules undergo nuclear relaxation within the singlet manifold of electronic states, the predominant spectral features shift to lower electron kinetic energy. The middle panel of Figure S4 shows an XPS spectrum from the $^1B_2$ state (which correlates to the $^1\Sigma_u$ at linear geometries) for which $\theta_{SCS} = 120°$. This overlaps entirely with the signal from ground-state CS_2 between 10 and 12 eV, and motivates our use of a decaying excited-state signal in our time-resolved fit described below. The middle panel in Figure S4 shows static spectra from both bent CS_2 and CS_2 with elongated CS bonds filling the region between 6 and 10 eV. Most of the spectral intensity in the mid-eKE region in Figure 2(b) of the main text therefore corresponds to molecular CS_2 undergoing large amplitude displacement, as well as CS fragments exhibiting elongated R_{CS} bonds (see the following section for more detail).

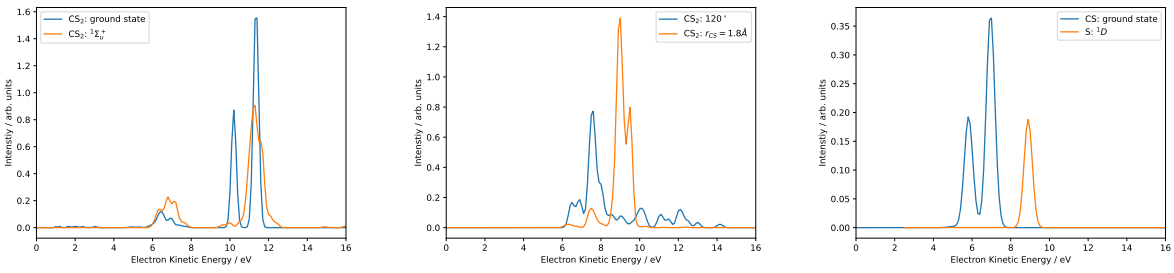

Figure S4: Static XPS spectra of CS_2, CS and S atomic fragments at key nuclear configurations: the $^1\Sigma_g$ ground state and $^1\Sigma_u$ excited state of CS_2 (left), the $^1B_1$ excited state with $\theta_{SCS} = 120°$ and $R_{CS} = 1.85$ Å (middle), and the $^1\Sigma_g$ of CS and ^1D of the S atom (right). The electron kinetic energy is given assuming ionization via a 181 eV photon.

As the molecule dissociates to CS and S products, intensity grows at low kinetic energy, corresponding to the region 5-6.5 eV in Figure 2(b) of the main text. The right panel of Figure S4 shows that this is primarily due to signal arising from the CS molecular fragment, with the atomic ^{1}D signal observed at higher kinetic energies. Additionally, the spin-orbit splitting between the S 2p lines in CS is clearly visible in the low-energy bands in the simulated TRXPS.

S3. Simulation of the Time-Resolved XPS Spectrum

The TRXPS spectrum was simulated by computing an XPS spectrum at the time-evolving centroid of the nuclear configuration of each trajectory basis function, in which the contribution of a trajectory to the total signal was weighted by the norm of the amplitude.

$$\sigma(E,t) = \sum_{I=1}^{N_s} \sum_{j=1}^{N_j^I} \left|C_j^I(t)\right|^2 \sigma_I\left(E; \bar{\boldsymbol{R}}_j^I(t)\right), \tag{S1}$$

Here $C_j^I(t)$ is the complex AIMS amplitude, and $\sigma_I\left(E_c; \bar{\boldsymbol{R}}_j^I(t)\right)$ is the ionization cross-section from neutral state I to the core-ionized state with energy E_c. This approach has been previously applied to the simulation of time-resolved core-absorption and valence photoelectron spectra.

The ground state bleach signal is presumed to be time-independent and was incorporated into the simulated TRXPS using the ground state static XPS signal shown in the left-most panel of Figure S4. The electron kinetic energy was obtained by taking the difference between 181.5 eV probe photon energy and calculated binding energies, with the latter shifted by 8.5 eV in order for the simulation to match the gas-phase CS_2 XPS spectrum.

Following the computation of each of the Dyson-orbital norms for each ionization channel at each trajectory centroid nuclear configuration and weighting by the trajectory basis function amplitude, the final spectrum in Figure 2(b) of the main text was obtained via

convolution with a 2D Gaussian function with a full width at half-maximum (FWHM) of 0.5 eV and 100 fs in the energy and time domains, respectively.

S4. Experimental Details

Experiments were performed at beamline BL1 of the FLASH free-electron laser[7] using the CAMP endstation,[8] operating as a dual-sided velocity-map imaging (VMI)[9] spectrometer. CS_2 was introduced into the spectrometer as a continuous supersonic molecular beam and collimated en route to the interaction region, where it was crossed nearly perpendicularly by co-propagating UV pump and X-ray probe pulses. The photoelectrons generated were mapped to a position-sensitive detector, comprising dual-stacked microchannel plates coupled to a phosphor screen, located at the bottom of the instrument. Electron hits were imaged using a CMOS camera. The recorded electron images represent two-dimensional projections of the underlying three-dimensional velocity distributions, and so, to extract photoelectron spectra, inverse Abel transformation was performed using the pBASEX algorithm.[10]

The 201.5 nm pump pulses were generated using the fourth harmonic of the FLASH pump-probe laser system, which consists of a Ti:sapphire oscillator and chirped pulse multipass amplifier (Coherent Inc., Hidra),[11] using the same scheme as employed previously at CAMP.[12] A motorized delay stage in the path of the 800 nm fundamental prior to the harmonic generation stages was used to vary the delay between the optical and FEL pulses. The 201.5 nm pulses had an estimated duration of 140 fs FWHM, with pulse energies of 200 nJ.

To probe the photodynamics of CS_2 from the S 2p site, the FLASH FEL photon energy was tuned to 181.5 eV. Typical on target pulse energies were 50 μJ, with an estimated pulse duration of 90 fs FWHM. Prior to delivery of the X-ray beam to the endstation and focusing into the instrument using Kirkpatrick-Baez mirrors, the X-ray pulses were characterised on a shot-to-shot basis. Pulse energies were measured using the FLASH gas monitor detector,[13]

while photon energy spectra were recorded using a variable line spacing spectrometer in the first order.[14] The jitter in the electron bunch arrival times was also recorded[15,16] and used in correcting the experimental pump-probe delays on a shot-by-shot basis.[17] Time zero was found by observing the prompt changes in the ion momentum distributions (not pictured here) measured in the ion side of the VMI apparatus. The time-resolved photoelectron spectrum was found by Abel-inverting the summed electron VMI image at each pump-probe delay, and the difference signal was calculated by subtracting the average photoelectron spectrum greater than 0.5 ps before time zero, shown in red in Figure 1(b) in the main text.

S5. Data Processing

The average spectrum of the FEL pulse is roughly of Gaussian shape, centered at 181.5 eV with a FWHM spread of 0.8 eV. This presents a challenge for energy resolution of the photoelectron spectrum if an average over all shots is performed. Fortunately, on a shot-by-shot basis, the spectrum is much narrower, and the mean photon energy jitter can also be corrected. In order to achieve sub-eV photoelectron resolution, we use only shots with a sufficiently narrow spectrum and perform a correction for the mean photon energy.

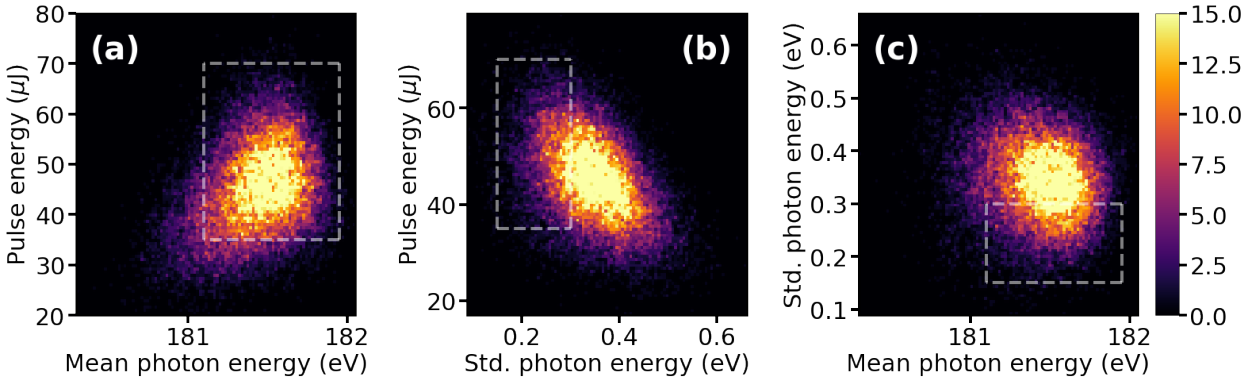

Figure S5: (a) Histogram of FEL pulse energy jointly with central photon energy. (b) Histogram of FEL pulse energy jointly with FEL pulse bandwidth (presented as a Gaussian standard deviation, "Std."). (c) Histogram of central photon energy jointly with FEL pulse bandwidth. Only the FEL shots falling within each of the dashed boxes were included in our analysis.

Figure S5 shows pairwise histograms of total pulse energy, central photon energy, and spectral width. The pulse energy and mean photon energy in Figure S5(a) show a slight correlation for low pulse energies, but the central lobe between 35 and 70 μJ is quite symmetric. A much stronger correlation can be seen in Figure S5(b) between the pulse energy and spectral width, with a clear tradeoff between pulse energy and bandwidth. Finally, the mean photon energy and spectral width show no clear correlation in Figure S5(c). Based on these histograms, we selected the following cuts, accepting only the data within the dashed white boxes in the figures: between 35 and 70 μJ, between 177.8 and 178.65 eV central photon energy, and below 0.3 eV spectral bandwidth. This eliminated pulses with few probe photons and with broad spectra, thus enhancing the spectral resolution and signal to noise of our TRXPS. Such a severe cut on the spectral bandwidth in particular meant that we rejected most of our collected data. However, we found that this selection balanced the upsides of narrower spectral bandwidth with the downsides of poorer statistics.

In order to account for the spread in mean photon energy among the pulses, we employed a shifting procedure based on several mean photon energy bins. Pulses were binned into ten equally spaced mean photon energy bins, shown in Figure S6(a), and the photoelectron spectrum for each bin was computed via Abel inversion, resulting in (for example) the family of curves shown in Figure S6(b). The legend labels of these spectra correspond to the shift of the mean photon energy bin used to compute that spectrum, relative to the lowest photon energy bin. The spectra were then shifted according to the mean photon energy of each bin and then summed, as shown in Figure S6(c). This helped to mitigate the jitter in mean FEL photon energy, further enhancing the energy resolution. By employing both a spectral bandwidth filter and a photon energy shifting procedure, we estimate that we achieve an energy resolution comparable to the upper limit on the bandwidth filter of $\sigma_{\mathrm{FEL}} = 0.3$ eV. This enabled us to partially resolve the two-peak structure of both ground-state CS_2 and the fragment CS due to spin-orbit splitting, an achievement that is comparable to results from spectral-domain ghost imaging ("spooktroscopy")[18,19] which are challenging to apply in this

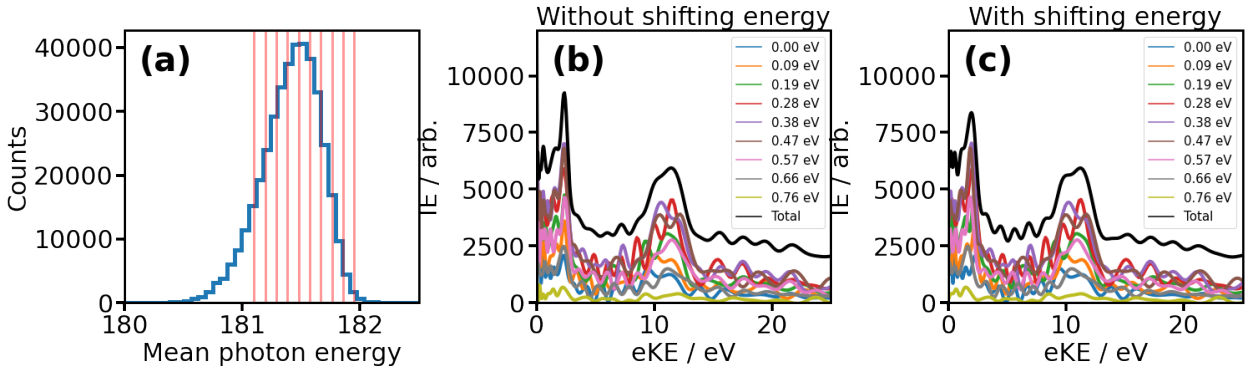

Figure S6: (a) Histogram of mean photon energy of all pulses, with mean photon energy bins illustrated as red lines. (b) The calculated photoelectron spectrum for each mean photon energy bin, without shifting applied. The legend labels correspond to the energy shift of the photon energy bin that was used to compute that spectrum. The total spectrum calculated by summing the individual spectra is shown in black to represent the photoelectron spectrum if no shifting is applied. (c) The same spectra with shifting applied based on the mean photon energy in each bin. The total summed spectrum is again shown in black, illustrating the sharpening of several peaks and the emergence of additional structure at low photoelectron energy.

time-resolved setting due to insufficient statistics.

Measurement uncertainties on the TRXPS signal were estimated via bootstrapping. Bootstrapping is a procedure where the entire dataset is sampled repeatedly with replacement, and the standard deviation in the quantity of interest after each sample is assigned as the uncertainty in the mean value measured using the entire dataset. In our case, we are interested in calculating a mean photoelectron spectrum, with the collection of all FEL shots comprising the collection of samples of this spectrum. To produce bootstrapped errorbars for the TRXPS signal, we repeatedly sample the set of shots that fall into each timebin with replacement, produce the summed electron VMI image, and Abel invert to produce the resampled photoelectron spectrum. This procedure is done repeatedly, and the standard deviation of this repeated resampling produces the errorbars seen in Figure 3 of the main text. Here in Figure S7 we show the magnitudes of the bootstrapped errorbars on the TRXPS signal. The uncertainties are roughly consistent across all timebins due to our relatively uniform distribution in the number of shots at all pump-probe delays. The uncertainties are larger at lower photoelectron energies simply because this energy region comprises a much

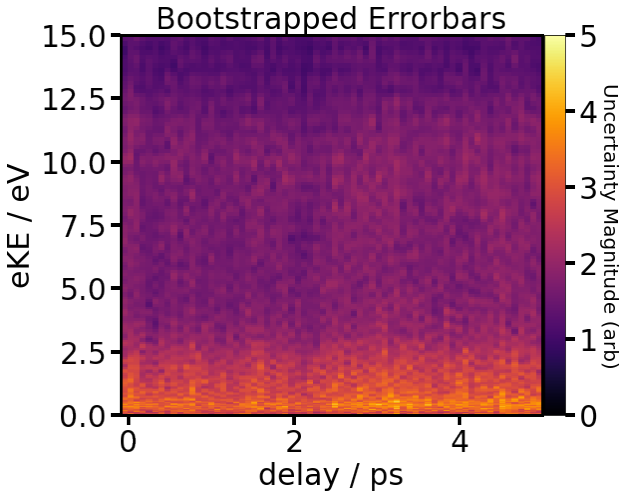

Figure S7: Bootstrapped uncertainties of the TRXPS signal. Uncertainty magnitudes are relative to the scale of the spectrum reported in Figure 1(b) of the main text.

smaller region on the electron VMI detector.

S6. Time-resolved Fitting

Time-resolved, energy-integrated signals within three electron kinetic energy (eKE) regions were fit to determine the characteristic timescales associated with each. The functional form of each energy integration region was informed by the expected behavior from the AIMS simulated signal, and generally employed an appropriate depletion of ground-state signal or growth of product signal, superimposed with an exponentially decaying excited-state signal. We thus refer to these fits collectively as the "Excited State Fit." The depletion region between 10.7 and 13 eV (Figure 2(c), blue line in the main text) consists of two features: a broad depletion of ground-state CS_2 signal, and a narrow enhancement in excited-state CS_2 signal that decays away as the molecule dissociates. The functional form used to fit this data was:

$$\begin{aligned} f_{\mathrm{dep}}(t;\tau_{\mathrm{IRF}},A_{\mathrm{dep}},\tau_{\mathrm{exc}},A_{\mathrm{exc}}) = A_{\mathrm{dep}} \cdot \left[1+\mathrm{erf}\left(\frac{t}{\sqrt{2}\tau_{\mathrm{IRF}}}\right)\right] \\ + \left\{U(t)\cdot A_{\mathrm{exc}}\exp\left(-\frac{t}{\tau_{\mathrm{exc}}}\right)\right\} \otimes G(t) \end{aligned} \tag{S2}$$

Here A_{dep} is the amplitude of the depletion, τ_{IRF} is the temporal instrument response function expressed as the Gaussian width of that depletion, A_{exc} is the amplitude of the excited state contribution, and τ_{exc} is the lifetime of that excited state. $U(t)$ is the Heaviside function, which sets all excited state contributions to zero for $t < 0$. $G(t)$ is a Gaussian cross-correlation function for the pump and probe lasers.

The regions of enhancement (Figure 2(c), red and green lines in the main text) were fit to slightly different functional forms to capture the growth of photoproduct signal in those eKE regions, as follows:

$$\begin{aligned} f_{\mathrm{exc}}(t;\tau_{\mathrm{exc}},A_{\mathrm{exc}},\tau_{\mathrm{prod}},A_{\mathrm{prod}}) = &\left\{U(t)\cdot A_{\mathrm{exc}}\exp\left(-\frac{t}{\tau_{\mathrm{exc}}}\right)\right\}\otimes G(t) \\ &+\left\{\left(1-U(t)\cdot A_{\mathrm{prod}}\exp\left(-\frac{t}{\tau_{\mathrm{prod}}}\right)\right)\right\}\otimes G(t) \end{aligned} \tag{S3}$$

Here A_{exc} and τ_{exc} are the amplitude and lifetime of the excited state signal, and A_{prod} and τ_{prod} are the amplitude and lifetime of the exponential rise of photoproduct signal. The results for these Excited State Fits are summarized in Table S1.

Table S1: Parameter values and uncertainties, along with goodness-of-fit values χ^2_ν, for the three Excited State Fits presented in the main text.

	Blue	Red	Green
τ_{IRF}	120 ± 50 fs (FWHM)		
A_{dep}	-3.48 ± 0.09		
τ_{exc}	830 ± 200 fs	90 ± 80 fs	
A_{exc}	2.4 ± 0.4	5.5 ± 4.7	
τ_{prod}		1220 ± 240 fs	490 ± 280 fs
A_{prod}		4.3 ± 0.2	1.61 ± 0.07
χ^2_ν	1.795	2.027	1.509

Our measure for goodness of fit was the reduced chi-squared χ^2_ν, or chi-squared per degree of freedom of the fit.

$$\chi^2_\nu = \frac{1}{\nu}\sum_{i=1}^{N_{\mathrm{obs}}}\frac{(x_i-\mu_i)^2}{\sigma_i^2} \tag{S4}$$

where $\nu = N_{\mathrm{obs}} - m_{\mathrm{param}}$ is the number of degrees of freedom of the fit in terms of the number

of observations N_{obs} and the number of free parameters in the fit m_{param}. A χ^2_ν value near 1 indicates a good fit, while a value much greater than 1 indicates the model describes the data poorly, and a value much less than 1 indicates over-fitting of the data. The χ^2_ν values for each of the fits are also reported in Table S1.

We also performed similar fits that included no contributions from any excited state ("Basic Fit"), and fits with a quantum beat in the excited state contributions ("Quantum Beat Fit"). For the Basic Fit, we employed a model similar to the ones described in Equations S2 and S3, but with the exponentially decaying excited state components removed. We also imposed the constraint that the instrument response function $\tau_{\text{IRF}}^{(\text{FWHM})}$ be less than 150 fs, which was the upper limit found at the experiment via temporal cross-correlation measurements. The Quantum Beat Fit was similar to the Excited State Fits but included the known 1010 fs quantum beat on the excited state signal due to the Fermi dyad splitting that was observed in prior work.[20] The functional form of the Quantum Beat Fits is shown below.

$$\begin{aligned} f_{\text{dep}}(t;\tau_{\text{IRF}},&A_{\text{dep}},\tau_{\text{exc}},A_{\text{exc}},A_{\text{beat}},\phi_{\text{beat}}) = \\ &A_{\text{dep}}\cdot\left[1+\text{erf}\left(\frac{t}{\sqrt{2}\tau_{\text{IRF}}}\right)\right] \\ &+\left\{U(t)\cdot A_{\text{exc}}\exp\left(-\frac{t}{\tau_{\text{exc}}}\right)\cdot\left[1+A_{\text{beat}}\cos\left(\frac{2\pi t}{1.01\text{ps}}+\phi_{\text{beat}}\right)\right]\right\}\otimes G(t) \end{aligned} \tag{S5}$$

$$\begin{aligned} f_{\text{exc}}(t;\tau_{\text{exc}},&\tau_{\text{prod}},A_{\text{prod}},A_{\text{beat}},\phi_{\text{beat}}) = \\ &\left\{U(t)\cdot A_{\text{beat}}\exp\left(-\frac{t}{\tau_{\text{exc}}}\right)\cos\left(\frac{2\pi t}{1.01\text{ps}}+\phi_{\text{beat}}\right)\right\}\otimes G(t) \\ &+\left\{\left(1-U(t)\cdot A_{\text{prod}}\exp\left(-\frac{t}{\tau_{\text{prod}}}\right)\right)\right\}\otimes G(t) \end{aligned} \tag{S6}$$

The quantum beat period of 1010 fs observed in[20] was fixed in these fits.

For each fit, we computed the same reduced chi-squared goodness-of-fit measure χ^2_ν described above in Equation S4. The best-fit parameter values of the Quantum Beat Fits are summarized in Table S2, while the best-fit parameter values of the Basic Fits are summa-

rized in Table S3. The Quantum Beat and Basic Fits are compared to the Excited State Fit below in Figure S8.

Table S2: Parameter values and uncertainties for the Quantum Beat Fits.

	Blue	Red	Green
A_{dep}	-3.5 ± 0.9		
τ_{IRF}	110 ± 40 fs (FWHM)		
τ_{exc}	760 ± 190 fs	560 ± 210 fs	
A_{beat}	0.4 ± 0.2	2.0 ± 0.5	
ϕ_{beat}	$0.5 \pm 0.4\ \pi$	$-0.28 \pm 0.08\ \pi$	
τ_{prod}		1170 ± 100 fs	490 ± 130 fs
A_{prod}		4.3 ± 0.1	1.61 ± 0.06
χ^2_ν	1.785	1.905	1.529

Table S3: Parameter values and uncertainties for the Basic Fits.

	Blue	Red	Green
A_{dep}	-3.15 ± 0.05		
τ_{IRF}	150 ± 60 fs (FWHM)		
τ_{prod}		150 ± 100 fs	460 ± 100 fs
A_{prod}		4.3 ± 0.1	1.60 ± 0.06
χ^2_ν	2.759	2.251	1.490

A comparison of the goodness-of-fit values for each type of model justifies our choice to use the Excited State Fit in the main text. For the depletion region (blue curves), both models that include an excited-state component have nearly identical χ^2_ν values of 1.79 and 1.78, while the Basic Fit has a much higher χ^2_ν value of 2.76. Although values greater than 1 indicate the model is doing a poor job of describing the data, the Excited State and Quantum Beat Fits clearly do a better job in this regard than the Basic Fit. This forms our justification for stating that we observe the dynamics of the $^1\Sigma_u^+$ state signal in our data.

The χ^2_ν values are more comparable for the mid-eKE enhancement (red curves) and nearly identical for the low-eKE enhancement (green curves). For the mid-eKE red region, the Quantum Beat Fit actually gives the best goodness-of-fit by a slight margin (1.90 vs 2.03 for the Excited State Fit), and is clearly distinguished from the Basic Fit at 2.25. We chose to include the Excited State Fit in this region in the main text for the sake of

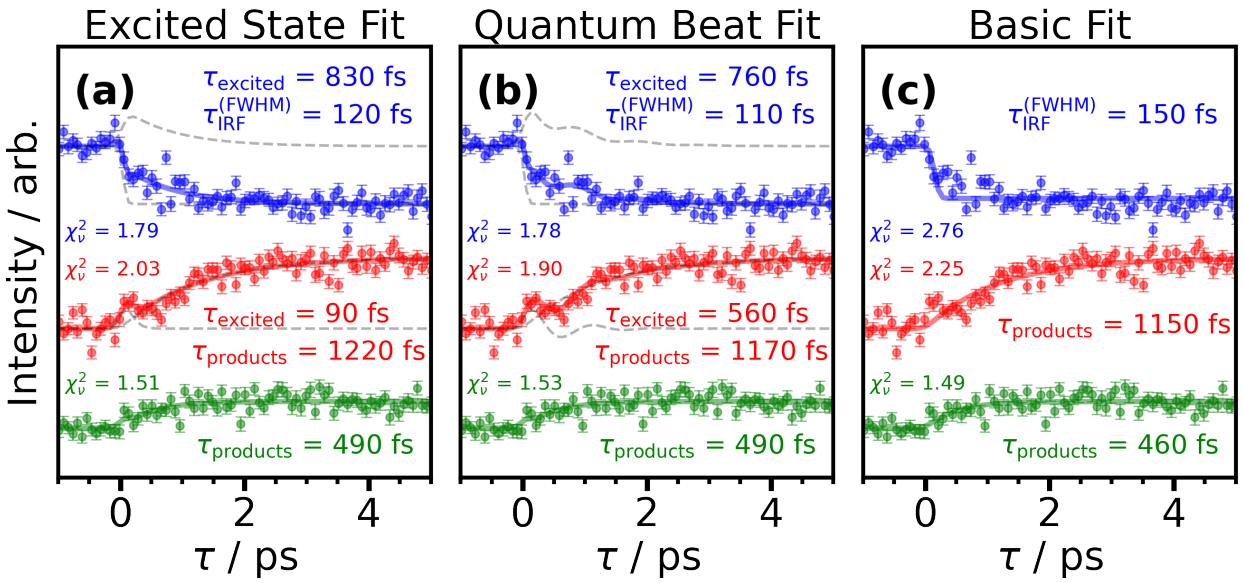

Figure S8: Comparison of three fits described above. For each fit, relevant timescale parameters-of-best-fit and the goodness-of-fit metric χ^2_ν are quoted in the corresponding color. The excited state and products/depletion components of the fits are shown in grey dashed lines. (a) Excited State Fit. (b) Quantum Beat Fit. (c) Basic Fit.

simplicity and because the Quantum Beat component may actually be fitting much more complex excited-state dynamics in this region. For the low-eKE green region, the three fits are indistinguishable, and so we report no contributions from any excited state in this region.

S7. Author Contributions

R.F. conceived the experiment, the plan for which benefited from further input from F.A., G.B., T.D., B.E., D.R. and M.S.. The electron spectrometer was prepared by B.E., A.T.N., C.C.P., C.P. and the photon spectrometer by G.B.. The optical laser setup was constructed by N.E. with further input from R.F.. The experiment was conducted onsite by G.B., H.B., N.E., B.E., D.G., E.G., S.K., A.T.N., C.C.P., C.P., A.Rod., A.Rou., A.Si., with online participation in the experiment by all coauthors. The experiment data was analyzed by F.A., M.Br., I.G., J.U. and the theoretical simulations performed by S.N., M.S. and I.S. Finally, F.A., I.G., R.F, D.R., M.S. and A.St. interpreted the results and wrote the manuscript with

input from all the authors.

References

(1) Schuurman, M. S.; Stolow, A. Dynamics at Conical Intersections. *Annu. Rev. Phys. Chem.* **2018**, *69*, 427–450.

(2) Wang, K.; McKoy, V.; Hockett, P.; Schuurman, M. S. Time-Resolved Photoelectron Spectra of CS_2: Dynamics at Conical Intersections. *Phys. Rev. Lett.* **2014**, *112*, 113007.

(3) Lischka, H.; Shepard, R.; Pitzer, R. M.; Shavitt, I.; Dallos, M.; Müller, T.; Szalay, P. G.; Seth, M.; Kedziora, G. S.; Yabushita, S.; Zhang, Z. High-Level Multireference Methods in the Quantum-Chemistry Program System COLUMBUS: Analytic MR-CISD and MR-AQCC Gradients and MR-AQCC-LRT for Excited States, GUGA Spin–Orbit CI and Parallel CI Density. *Phys. Chem. Chem. Phys.* **2001**, *3*, 664–673.

(4) Karlström, G.; Lindh, R.; Malmqvist, P.-Å.; Roos, B. O.; Ryde, U.; Veryazov, V.; Widmark, P.-O.; Cossi, M.; Schimmelpfennig, B.; Neogrady, P.; Seijo, L. MOLCAS: A Program Package for Computational Chemistry. *Computational Materials Science* **2003**, *28*, 222–239.

(5) Epifanovsky, E. et al. Software for the Frontiers of Quantum Chemistry: An Overview of Developments in the Q-Chem 5 Package. *The Journal of Chemical Physics* **2021**, *155*, 084801.

(6) Schuurman, M. S.; Blanchet, V. Time-Resolved Photoelectron Spectroscopy: The Continuing Evolution of a Mature Technique. *Phys. Chem. Chem. Phys.* **2022**, *24*, 20012–20024.

(7) Ackermann, W. et al. Operation of a Free-Electron Laser from the Extreme Ultraviolet to the Water Window. *Nat. Photonics* **2007**, *1*, 336–342.

(8) Erk, B. et al. CAMP@FLASH: An End-Station for Imaging, Electron- and Ion-Spectroscopy, and Pump–Probe Experiments at the FLASH Free-Electron Laser. *J. Synchrotron Radiat.* **2018**, *25*, 1529–1540.

(9) Eppink, A. T. J. B.; Parker, D. H. Velocity Map Imaging of Ions and Electrons Using Electrostatic Lenses: Application in Photoelectron and Photofragment Ion Imaging of Molecular Oxygen. *Rev. Sci. Instrum.* **1997**, *68*, 3477–3484.

(10) Garcia, G. A.; Nahon, L.; Powis, I. Two-Dimensional Charged Particle Image Inversion Using a Polar Basis Function Expansion. *Review of Scientific Instruments* **2004**, *75*, 4989–4996.

(11) Redlin, H.; Al-Shemmary, A.; Azima, A.; Stojanovic, N.; Tavella, F.; Will, I.; Düsterer, S. The FLASH Pump–Probe Laser System: Setup, Characterization and Optical Beamlines. *Nucl. Instrum. Meth. A* **2011**, *635*, S88 – S93.

(12) Forbes, R.; Allum, F.; Bari, S.; Boll, R.; Borne, K.; Brouard, M.; Bucksbaum, P. H.; Ekanayake, N.; Erk, B.; Howard, A. J., et al. Time-Resolved Site-Selective Imaging of Predissociation and Charge Transfer Dynamics: The CH_3I B-band. *J. Phys. B: At. Mol. Opt. Phys.* **2020**, *53*, 224001.

(13) Tiedtke, K. et al. Gas Detectors for X-Ray Lasers. *J. Appl. Phys.* **2008**, *103*, 094511.

(14) Brenner, G.; Kapitzki, S.; Kuhlmann, M.; Ploenjes, E.; Noll, T.; Siewert, F.; Treusch, R.; Tiedtke, K.; Reininger, R.; Roper, MD., et al. First Results from the Online Variable Line Spacing Grating Spectrometer at FLASH. *Nuclear Instruments and Methods in Physics Research Section A: Accelerators, Spectrometers, Detectors and Associated Equipment* **2011**, *635*, S99–S103.

(15) Löhl, F.; Arsov, V.; Felber, M.; Hacker, K.; Jalmuzna, W.; Lorbeer, B.; Ludwig, F.; Matthiesen, K.-H.; Schlarb, H.; Schmidt, B.; Schmüser, P.; Schulz, S.; Szewinski, J.;

Winter, A.; Zemella, J. Electron Bunch Timing with Femtosecond Precision in a Superconducting Free-Electron Laser. *Phys. Rev. Lett.* **2010**, *104*, 144801.

(16) Schulz, S. et al. Femtosecond All-Optical Synchronization of an X-ray Free-Electron Laser. *Nat. Commun.* **2015**, *6*, 5938.

(17) Savelyev, E.; Boll, R.; Bomme, C.; Schirmel, N.; Redlin, H.; Erk, B.; Düsterer, S.; Müller, E.; Höppner, H.; Toleikis, S., et al. Jitter-Correction for IR/UV-XUV Pump-Probe Experiments at the FLASH Free-Electron Laser. *New J. Phys.* **2017**, *19*, 043009.

(18) Li, S.; Driver, T.; Alexander, O.; Cooper, B.; Garratt, D.; Marinelli, A.; P. Cryan, J.; P. Marangos, J. Time-Resolved Pump–Probe Spectroscopy with Spectral Domain Ghost Imaging. *Faraday Discuss.* **2021**, *228*, 488–501.

(19) Wang, J.; Driver, T.; Allum, F.; Papadopoulou, C. C.; Passow, C.; Brenner, G.; Li, S.; Düsterer, S.; Noor, A. T.; Kumar, S.; Bucksbaum, P. H.; Erk, B.; Forbes, R.; Cryan, J. P. Photon Energy-Resolved Velocity Map Imaging from Spectral Domain Ghost Imaging. *New J. Phys.* **2023**, *25*, 033017.

(20) Bisgaard, C. Z.; Clarkin, O. J.; Wu, G.; Lee, A. M. D.; Geßner, O.; Hayden, C. C.; Stolow, A. Time-Resolved Molecular Frame Dynamics of Fixed-in-Space CS_2 Molecules. *Science* **2009**, *323*, 1464–1468.